Commun. Comput. Phys.
doi: 10.4208/cicp.250311.081211a

Vol. **12**, No. 4, pp. 1096-1120
October 2012

AUSM-Based High-Order Solution for Euler Equations

Angelo L. Scandaliato[1] and Meng-Sing Liou[2,*]

[1] *Ohio Aerospace Institute, Cleveland, OH, 44142, USA.*[†]
[2] *NASA Glenn Research Center, Cleveland, OH, 44135, USA.*

Received 25 March 2011; Accepted (in revised version) 8 December 2011

Communicated by Kun Xu

Available online 17 April 2012

Abstract. In this paper we demonstrate the accuracy and robustness of combining the advection upwind splitting method (AUSM), specifically AUSM$^+$-UP [9], with high-order upwind-biased interpolation procedures, the weighted essentially non-oscillatory (WENO-JS) scheme [8] and its variations [2,7], and the monotonicity preserving (MP) scheme [16], for solving the Euler equations. MP is found to be more effective than the three WENO variations studied. AUSM$^+$-UP is also shown to be free of the so-called "carbuncle" phenomenon with the high-order interpolation. The characteristic variables are preferred for interpolation after comparing the results using primitive and conservative variables, even though they require additional matrix-vector operations. Results using the Roe flux with an entropy fix and the Lax-Friedrichs approximate Riemann solvers are also included for comparison. In addition, four reflective boundary condition implementations are compared for their effects on residual convergence and solution accuracy. Finally, a measure for quantifying the efficiency of obtaining high order solutions is proposed; the measure reveals that a maximum return is reached after which no improvement in accuracy is possible for a given grid size.

AMS subject classifications: 65, 76

Key words: Shock capturing, advection upwind splitting, Euler equations, weighted essentially non-oscillatory, monotonicity preserving.

1 Introduction

The complete procedure for solving time-dependent partial differential equations of conservations laws with upwind schemes in the finite-volume setting consists of three basic

*Corresponding author. *Email addresses:* ascandal@ucsd.edu (A. L. Scandaliato), meng-sing.liou@nasa.gov (M.-S. Liou)
[†]Currently, University of California at San Diego.

steps: reconstruction, flux evaluation, and time integration. The boundary condition is included as part of the flux evaluation before the solution in the whole domain is time-advanced. There have been enormous studies done for improving methodologies in each step. As each step provides the data needed for the next step, it is expected that different results should surface for different combinations of methods for each step. In recent years high order interpolations have received increased interest after years of successful applications using first, second, and even third order high-resolution shock-capturing methods. In this study, we intend to investigate the effectiveness on accuracy, robustness, and efficiency, of combining the advection upstream splitting method (AUSM) [13], especially its recent all-speed version AUSM$^+$-UP [9], with two high order concepts, the weighted essentially non-oscillatory (WENO-JS) scheme [8] and the monotonicity preserving (MP) scheme [16]. Both use a high order interpolant for smooth flow and modify it when encountering discontinuities. Basically, WENO attempts to modify the interpolant by re-weighting sub-interpolants, and MP limits the value of interpolated data through criteria such as monotonicity and extrema preservation. We shall also include recent variants of the original WENO, WENO-M [7] and WENO-Z [2], for comparison.

The first step, reconstruction, provides two data sets obtained by interpolating solution data from cell center to cell edge locations in a directionally biased manner. The crucial requirement is to ensure that no extra oscillations are generated numerically; a strong statement is the so-called total variation diminishing (TVD) property put forth by Harten [5]. The two data sets, typically denoted as the "left" and "right" states, are the input to the evaluation of flux at the cell edges, formulated as the Riemann problem in a finite domain.

The second step, flux evaluation, perhaps contributing to the most diverse area of research in the upwind scheme, maps the state data to numerical fluxes that result in the spatial balance of fluxes through the volume faces. This step critically influences the solution accuracy and past studies have resulted in several prominent and widely-used flux schemes.

The last step, time integration, uses the numerical fluxes to advance the solution in time. A successful method for time advancement must promote accuracy, convergence, stability, efficiency, and ease of use. From an implementation standpoint, there are two major approaches for these types of methods: implicit and explicit. Implicit methods use numerical fluxes from time levels where the solution is unknown for advancement and require an efficient solution of a large matrix-vector equation. Explicit methods only use numerical fluxes from previous time levels for advancement and are calculated directly. The choice of time advancement strategy typically will have the most profound effect on the allowable range of time step size that maintains numerical stability. For our purposes, all included results are calculated using the explicit third order TVD Runge-Kutta method [15], denoted as RK3.

In Section 2, the well-known high order interpolation procedures of the weighted essentially non-oscillatory (WENO) method and the monotonicity preserving (MP) method are outlined. Afterwards, two strategies are outlined for reducing the order of the in-

terpolation to prevent non-physical values; e.g. negative density or pressure. Section 3 extends the discussion of Section 2 for the system of 2D Euler equations and discusses the choice of primitive, conservative, or characteristic variables used in the interpolation. In Section 4, the upwind biased interpolated variables are combined with an approximate Riemann solver. The advection upwind splitting method (AUSM-family) is outlined with specific detail for the AUSM$^+$-UP version, which is appropriately scaled with added dissipation terms. Special attention is given for a slight procedural modification depending on whether the problem is unsteady or steady. Comparisons are made with Roe's scheme with an entropy fix and the Lax-Friedrichs scheme. Section 5 investigates four types of reflective boundary condition implementations and their effects on overall convergence to a steady state. The solution quality is discussed in detail for the problems of Sod, oblique-shock reflection, double Mach reflection, Rayleigh-Taylor instability, and shock diffraction around a 90-degree corner. Lastly, a quantitative measure is suggested to evaluate the efficiency of a high-order interpolation scheme in terms of accuracy (convergence) and computational time.

2 High order interpolations

In order to achieve high order accuracy, while maintaining monotonicity in the presence of discontinuities, nonlinear methods must be utilized [4]. Nonlinear approximations are dependent on the solution data and therefore must have a mechanism to automatically adapt during runtime. The goal is to give a sharp representation of discontinuities and simultaneously avoid creating Gibbs phenomenon-like numerical oscillations. All nonlinear methods investigated during this study are based on adaptations of basic linear methods.

In this section, the performance of two high order nonlinear interpolation methods are outlined; they are the WENO and MP methods, briefly summarized below. The cited references contain fully detailed development for these methods. Although both WENO and MP are derived from a geometric standpoint, their overall methodologies vary considerably. The WENO procedure uses an adaptive stencil to reduce oscillations, while MP limits the allowable range of interpolated data. Because increased order often can produce non-physical negative density and pressure values, reduction methods that locally reduce the order of accuracy are needed in practice. The desire to continue increasing order of accuracy must be addressed in two contexts: resolution of flow features of various length scales and computing cost. Timing tests are completed to compare each procedure's computational cost versus accuracy gain.

2.1 WENO

The original weighted essentially non-oscillatory (WENO) method (Liu et al., 1994) and its subsequent variations reduce the influence of any interpolation stencil that contains

a discontinuity. This is accomplished by adaptively combining linear non-compact sub-stencils using adjustable solution-dependent weights. The outcome is a final nonlinear non-compact stencil. The final stencil is referred to as nonlinear because it is dependent on solution values through the dynamic weights. In smooth regions the final stencil approaches an optimal stencil of high accuracy and high resolution. Near discontinuities, linear sub-stencils that contain the least amount of variation in solution values, i.e. the smoothest linear sub-stencils, are given more weight and subsequently the final nonlinear stencil is biased toward one side of the jump location. The intelligence, and majority of the cost, resides in calculating the dynamic weights with an indicator of smoothness for each sub-stencil. There has been significant testing and improvements since the original WENO scheme; notably a finite difference formulation by [8] denoted as WENO-JS, a more efficient indicator of smoothness version denoted as WENO-Z [2], and a mapped nonlinear weight version denoted as WENO-M [7]. Both WENO-Z and WENO-M show that a less dissipative version of WENO must use solution data that cross discontinuities to a certain extent. Concerning the concept and detailed procedure of the family of WENO schemes, the interested reader is highly recommended to refer to the cited papers above.

In this study, we specifically focused on three WENO variations, namely WENO-JS, WENO-Z and WENO-M. Contrary to common belief, WENO-Z seeks to augment (not avoid) the influence of sub-stencils containing discontinuities, hence substantially increasing their weights relative to those associated with smooth stencils. Its computational cost is on par with the WENO-JS, but the WENO-M is slightly more expensive due to an extra mapping function. However, for higher than 5^{th}-order, WENO-Z becomes increasingly unstable and admits oscillatory behavior. A remedy is to increase the exponential parameter p used in determining weights so as to provide more dissipation near critical points.

In both the WENO-Z and WENO-M formulations, a small parameter ε must be added to avoid a division by zero and $\varepsilon = 10^{-40}$ has been used with satisfactory results.

2.2 MP

The monotonicity-preserving (MP) method [16] adaptively limits the allowable range of the interpolation function. A linear non-compact or compact stencil is used to provide a baseline (provisional) smooth interpolation that is later bounded to a dynamically specified range. The objective of the MP scheme is to determine solution dependent bounds that strike a balance between maintaining high order accuracy and monotonicity. The limiter provides an interval determined by first order bounds for monotone solution regions. On non-monotone regions, the interval is enlarged to avoid cutting off local extrema, thereby preserving accuracy. The main difference between the WENO and MP methods for sensing smoothness of the solution is that MP uses simple difference operators, making it substantially cheaper than WENO to compute and the cost relatively insensitive to the increase in accuracy.

2.3 Recursive order reduction and simple extra limiting

Although the high-order nonlinear interpolations investigated make large strides in promoting monotonicity, they do not have any built-in mechanism that will guarantee the positivity of density and pressure. Ideally, the interpolation should maintain positivity of density and pressure a priori. More generally, greater confidence in the entire upwind scheme could be achieved if all prior constraints, such as positivity, were maintained a priori. Alternatively two common a posteriori techniques to prevent non-positive densities and pressures are simple extra limiting (SEL) and the recursive order reduction (ROR) [3], both of which create an unfortunate consequence of losing accuracy locally.

For the SEL method, replace any non-positive values of density and pressure by a small positive arbitrary constant, 10^{-5} in our tests. The SEL correction significantly reduces accuracy at locations where it must be used. The ROR correction sequentially reduces the order of the interpolation until a satisfactory value is achieved and in the worst case will default to first order, which always preserves monotonicity and positivity. If used too often, SEL and ROR could significantly reduce the overall solution quality. Therefore, it is important to track all locations where the posteriori positivity corrections are used.

2.4 Timing test

Fig. 1 displays the timing results for the three interpolation schemes given above (WENO-Z, WENO-M, and MP), computed from third to thirteenth order. The MP procedure is in general an order of magnitude faster than the WENO variations and the increase in time with the order of accuracy is much milder. This is because the MP limiting procedure is independent of the order of accuracy and the main cause of increased runtime lies in calculating the original (baseline) high order solution. Hence, MP is an attractive method for very high order accuracy. In contrast, the WENO procedure becomes substantially more expensive as order increases, as also noted in [1]. The timings were done on a Intel® Core^{TM}2 Duo CPU T9300 @ 2.50GHz, 1GB RAM, with Microsoft Windows XP operating system.

3 Interpolated variables

Three sets of variables are commonly used for interpolation: primitive, conservative, and characteristic variables. Past results show that the interpolation of primitive or conservative variables is prone to creating over/under shoots near strong discontinuities or near reflecting boundaries. Alternatively, one could interpolate the flux quantities directly. However, this presents a difficulty since the Riemann solvers operate on primitive variables and transforming the newly interpolated flux quantities back to primitive variables gives double roots. It is unclear which root will be physically valid. This leaves the characteristic variables as the preferred choice, also confirmed by the results shown here; but

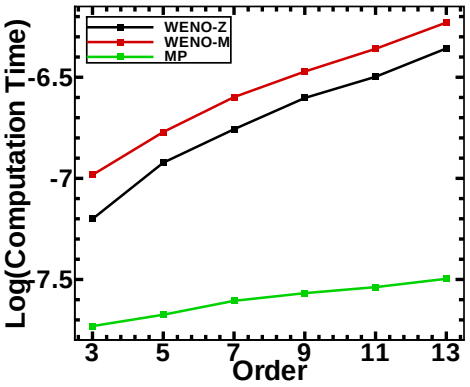

Nonlinear Interpolation Timing (seconds)			
Order	**WENO-Z**	**WENO-M**	**MP**
3^{rd}	6.29868e-008	1.04053e-007	1.85952e-008
5^{th}	1.19534e-007	1.6949e-007	2.11623e-008
7^{th}	1.74913e-007	2.52257e-007	2.47911e-008
9^{th}	2.49772e-007	3.37417e-007	2.70548e-008
11^{th}	3.17925e-007	4.37083e-007	2.89785e-008
13^{th}	4.39019e-007	5.89446e-007	3.18699e-008

Figure 1: Interpolation timing tests for WENO-M, WENO-Z and MP for accuracy from 3^{rd} to 11^{th} order, MP is substantially cheaper and the gap increases with the order of accuracy.

some ambiguity arises in defining the transformation matrix between variables.

This section extends the interpolations of the previous section to solve the Euler equations governing the flow of an inviscid compressible ideal gas. The hyperbolic, i.e. having a complete set of real eigenvalues, nature of the system is utilized in defining characteristic variables that will be used in interpolation because they form an independent set of equations.

In Cartesian coordinates the 2D Euler equations are expressed as:

$$\frac{\partial U}{\partial t}+\frac{\partial F}{\partial x}+\frac{\partial G}{\partial y}=0, \tag{3.1}$$

$$V=\begin{bmatrix}\rho\\ u\\ v\\ p\end{bmatrix},\quad U=\begin{bmatrix}\rho\\ \rho u\\ \rho v\\ E\end{bmatrix},\quad F=\begin{bmatrix}\rho u\\ \rho u^2+p\\ \rho uv\\ u(E+p)\end{bmatrix},\quad G=\begin{bmatrix}\rho v\\ \rho uv\\ \rho v^2+p\\ v(E+p)\end{bmatrix}, \tag{3.2}$$

where the total energy is

$$E=\frac{p}{(\gamma-1)}+\frac{\rho(u^2+v^2)}{2}. \tag{3.3}$$

In the above system, ρ is the density, $\vec{q}=\langle u,v\rangle$ is the velocity vector, p is the pressure, and $\gamma=1.4$ is the ratio of specific heats. The vector quantities V, U, F, and G, are known as the primitive variables, conservative variables, x-directional and y-directional fluxes respectively.

To use characteristic variables as the basis for interpolation, one begins the derivation by first converting the hyperbolic conservation law into a non-conservation form

$$\frac{\partial U}{\partial t}+\mathrm{J_F}\frac{\partial U}{\partial x}+\mathrm{J_G}\frac{\partial U}{\partial y}=0, \tag{3.4}$$

where $J_F = \partial F/\partial U$ and $J_G = \partial G/\partial U$ are flux Jacobian matrices with all real eigenvalues. Since Eq. (3.1) is hyperbolic, the Jacobian matrices are diagonalizable and admit the eigen-systems

$$L_F J_F R_F = \Lambda_F, \tag{3.5}$$

and

$$L_G J_G R_G = \Lambda_G, \tag{3.6}$$

where the L's, R's, and Λ's are matrices comprising row-wise left eigenvectors, column-wise right eigenvectors satisfying $L^{-1} \equiv R$, and diagonal eigenvalues respectively. Since the multidimensional Eq. (3.4) does not permit simultaneous diagonalization, the standard approach is followed in which the system will be considered on a dimension-by-dimension basis. Hence, it suffices to consider each dimension separately, thus neglecting the y-component in the remainder of this section. By replacing J_F in Eq. (3.4) with its eigen-system decomposition, Eq. (3.5), we have

$$L_F \frac{\partial U}{\partial t} + \Lambda_F L_F \frac{\partial U}{\partial x} = 0. \tag{3.7}$$

A similar expression is encountered for the y-direction. At the discrete level, matrix L_F is linearized about some local neighborhood in terms of U or V, denoted by $\tilde{L}_F$, to achieve the diagonalized system

$$\frac{\partial (W_F)}{\partial t} + \Lambda_F \frac{\partial (W_F)}{\partial x} = 0, \tag{3.8}$$

where $W_F = \tilde{L}_F U$ are known as the characteristic variables. Since Λ_F is a diagonal matrix, Eq. (3.8) admits a decoupled linearized system for the variables W_F.

The local linearization $\tilde{L}_F$ used to define the characteristic variables is not unique. It is common to use the state just to the left of the interface to linearize the left stencil and the state just to the right of the interface to linearize the right stencil, hereafter this choice is referred to as local characteristic-variables interpolation. An alternative method is to define an average state, e.g. Roe-average or algebraic-average, about which both the left and right stencils are linearized. While employing the characteristic variables facilitates the extension of high order interpolation procedures for a scalar equation to the system of equations, it creates the need for specifying the linearization. The linearization procedure becomes deeply intertwined in the calculations and could make the scheme unstable. Moreover, because of the local nature of the linearization, it is preferable to use smaller stencils rather than larger ones.

Fig. 2 shows that when primitive variables are interpolated for the 1D Sod Problem, an overshoot appears when the shock first forms, and more severe oscillations develop when it reflects off the wall boundary. Interpolation of characteristic variables on the other hand does not have these issues; the use of local characteristic-variables in linearization has a slight edge over the Roe-average states. In these results, the normal velocity component is set equal to zero at the wall in the implementation with ghost

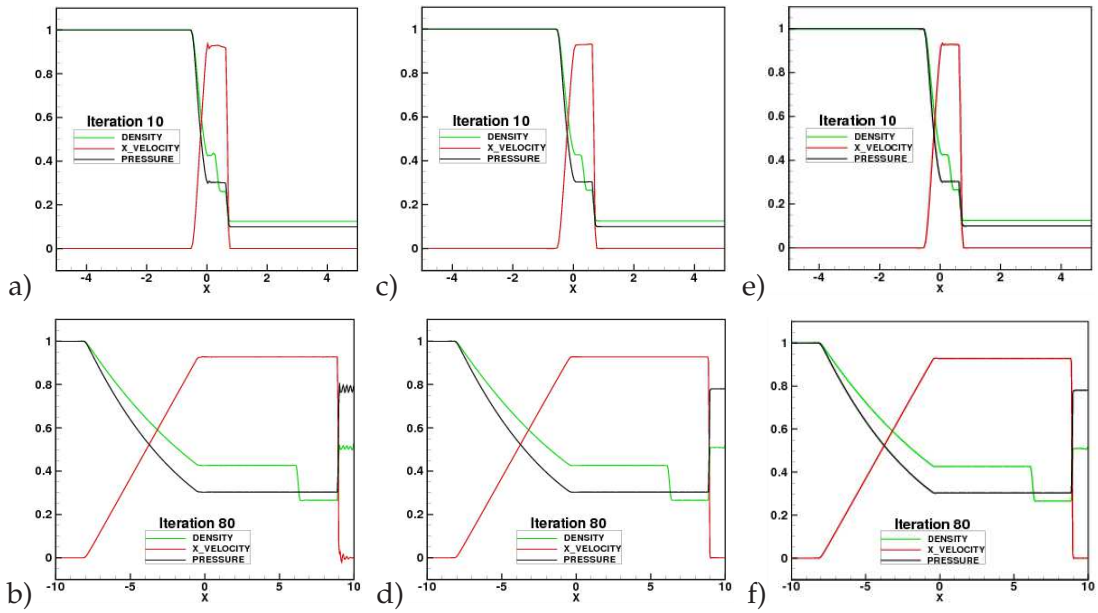

Figure 2: Evaluation of variables employed in the interpolation for solving the 1D Sod problem. 1^{st} column: primitive variables interpolation; 2^{nd} column: characteristic variables interpolation; 3^{rd} column: characteristic variables interpolation using Roe-average states. All with normal velocity component set equal to 0. Top row, a), c) & e),: the results shortly after breaking diaphragm. Bottom row, b), d) & f): the results shortly after reflection of shock wave off the wall.

cells; the results using boundary condition in [12] give the same conclusion concerning the variables used.

4 AUSM$^+$-UP

In the majority of WENO papers, the dissipative Lax-Friedrichs scheme has been employed and only some use other less dissipative numerical fluxes. To the best of our knowledge, there has not been a detailed attempt of studying the performance of AUSM-family in combination with high order methods. It is our objective to demonstrate that high order interpolations can be achieved with AUSM-family schemes with ease and robustness for complex problems. In particular, the procedure for the most recent version of the AUSM-family, AUSM$^+$-UP [9], is outlined and the reader is referred to the cited reference for details.

There has been many extensions from the original AUSM scheme [10, 12, 13]. AUSM-family fluxes have been developed as an alternative for two other well-known approaches, namely the flux vector splitting (FVS) and flux difference splitting (FDS), by attaining their respective advantages and avoiding disadvantages. The AUSM$^+$-UP solver, designed to be valid for all speeds, properly scales an added dissipation term with flow speed. For steady flows, this dissipation is optimized by the use of a scaling factor pro-

portional to the pressure difference at the cell interface. The result, as will be seen later, is that it eliminates oscillations seen near the boundary where the transverse velocity component is diminishing.

Step-by-step algorithm for AUSM$^+$-UP:

1. Prepare the left (L) and right (R) states in the form of primitive variables (V); for higher order interpolation of characteristic variables (W) as described in the previous section, a conversion, $W \mapsto V$, is needed.

$$V_L=[\rho_L,u_L,v_L,p_L]^T, \qquad V_R=[\rho_R,u_R,v_R,p_R]^T. \tag{4.1}$$

2. Calculate velocity components normal to a cell interface (1/2), whose unit normal vector being $\vec{n}=\langle n_x,n_y\rangle$, and total enthalpy,

$$q_L=u_Ln_x+v_Ln_y, \qquad q_R=u_Rn_x+v_Rn_y, \tag{4.2}$$

$$H_L=\frac{\gamma p_L}{(\gamma-1)\rho_L}+\frac{{u_L}^2+{v_L}^2}{2}, \qquad H_R=\frac{\gamma p_R}{(\gamma-1)\rho_R}+\frac{{u_R}^2+{v_R}^2}{2}. \tag{4.3}$$

3. Calculate interface speed of sound $a_{1/2}$,

$$a_L^*=\left(\frac{2(\gamma-1)}{\gamma+1}H_L\right)^{1/2}, \qquad a_R^*=\left(\frac{2(\gamma-1)}{\gamma+1}H_R\right)^{1/2}, \tag{4.4}$$

$$a_{1/2}=\max\left(\frac{{a_L^*}^2}{\max\left(a_L^*,q_L\right)},\frac{{a_R^*}^2}{\max\left(a_R^*,(-q_R)\right)}\right). \tag{4.5}$$

4. Calculate left and right normal Mach numbers,

$$M_L=\frac{q_L}{a_{1/2}}, \qquad M_R=\frac{q_R}{a_{1/2}}. \tag{4.6}$$

5. Calculate split Mach number and pressure polynomials to define interface normal velocity and pressure. Let

$$\mathcal{M}_{(1)}^{\pm}(M)=\frac{1}{2}(M\pm|M|), \qquad \text{and} \quad \mathcal{M}_{(2)}^{\pm}(M)=\pm\frac{1}{4}(M\pm1)^2, \tag{4.7}$$

then the split "positive" and "negative" Mach numbers and pressures are defined as:

$$\mathcal{M}_{(4)}^{\pm}(M)=\begin{cases}\mathcal{M}_{(1)}^{\pm}(M), & \text{if } |M|\geq1,\\ \mathcal{M}_{(2)}^{\pm}(M)(1\mp2\mathcal{M}_{(2)}^{\mp}(M)), & \text{otherwise}\end{cases} \tag{4.8}$$

and

$$\mathcal{P}_{(5)}^{\pm}(M)=\begin{cases}\frac{1}{M}\mathcal{M}_{(1)}^{\pm}(M), & \text{if } |M|\geq1,\\ \mathcal{M}_{(2)}^{\pm}(M)[(\pm2-M)\mp3M\mathcal{M}_{(2)}^{\mp}(M)], & \text{otherwise.}\end{cases} \tag{4.9}$$

These are the ingredients needed to accomplish the AUSM$^+$ [10]. The following steps, (6)-(8), constitute the velocity (u) and pressure (p) diffusion terms used in the AUSM$^+$-UP [9].

6. Calculate a reference Mach number M_o. First define an average interface Mach number

$$\overline{M^2} = (M_L^2 + M_R^2)/2 \tag{4.10}$$

and a global maximum face-normal Mach number‡

$$M_{max}^2 = \max_{\forall\ i,j} \left[\frac{un_x + vn_y}{a} \right]_{i,j}^2. \tag{4.11}$$

Then

$$M_o^2 = \min(1, \max(\overline{M^2}, M_{max}^2)) \in [0,1]. \tag{4.12}$$

7. Calculate a scaling function,

$$f_a(M_o) = M_o(2 - M_o) \in [0,1]. \tag{4.13}$$

8. Choose a representative interface density, e.g.,

$$\rho_{1/2} = (\rho_R + \rho_L)/2. \tag{4.14}$$

9. Obtain interface Mach number,

$$M_{1/2} = \mathcal{M}_{(4)}^+(M_L) + \mathcal{M}_{(4)}^-(M_R) - \frac{K_p}{f_a} \max(1 - \overline{M^2}, 0) \frac{p_R - p_L}{\rho_{1/2} a_{1/2}^2} \tag{4.15}$$

and interface pressure

$$p_{1/2} = \mathcal{P}_{(5)}^+(M_L) + \mathcal{P}_{(5)}^-(M_R) - 2K_u \mathcal{P}_{(5)}^+ \mathcal{P}_{(5)}^- \rho_{1/2} (f_a a_{1/2})(q_R - q_L) \tag{4.16}$$

with default setting of $K_p = 0.25$ and $K_u = 0.75$.

10. Finally the numerical interface flux is evaluated by upwinding,

$$F_{1/2} = a_{1/2} M_{1/2} \begin{cases} \Phi_L, & \text{if } M_{1/2} > 0, \\ \Phi_R, & \text{otherwise} \end{cases} + p_{1/2} N_{1/2}, \tag{4.17}$$

where

$$\Phi = [\rho, \rho u, \rho v, \rho H]^T, \qquad N = [0, n_x, n_y, 0]^T. \tag{4.18}$$

The first two terms in equations for $M_{1/2}$ and $p_{1/2}$ are common amongst all AUSM-family schemes. They are directionally-biased split Mach numbers $\mathcal{M}_{(4)}^+(M)$ and $\mathcal{M}_{(4)}^-(M)$, and split pressures $\mathcal{P}_{(5)}^+(M)$ and $\mathcal{P}_{(5)}^-(M)$; they are constructed using the eigenvalues $(u \pm a)$ associated with nonlinear fields; see [10]. Here, the subscript is the order of the polynomial and the superscript represents the direction indicative of the sign of eigenvalue. Although the use of split Mach numbers, such as $\mathcal{M}_{(4)}^{\pm}(M)$, is reminiscent of Van Leer's flux vector splitting, the introduction of the interface Mach number $M_{1/2}$

‡The following steps, Eqs. (4.11)-(4.13), can be skipped if an unsteady flow is considered, by setting $f_a = 1$ for Eq. (4.13).

is a major departure, making the AUSM-family as accurate as FDS for computing contact discontinuity and viscous layers. The last term in the equations for $M_{1/2}$ and $p_{1/2}$ is the adaptive dissipation that couples the velocity and pressure. Notice the use of a reference Mach number M_o in the determination of the scaling function $f_a(M_o)$, which is especially crucial for providing a proper amount of dissipation in *steady* low Mach flow regime. For *unsteady* flows $f_a=1$ and there is no need to calculate $M_{\max}$ and M_o, i.e., skipping Eqs. (4.11)-(4.13). The parameter values chosen for (K_p,K_u) were determined based on tests on model problems in Liou's previous work and have been found to perform well for a variety of problems.

Previous work has been focused on combining WENO or MP with dissipative Riemann solvers, most notably the Lax-Friedrichs method. Meanwhile much work using more accurate flux schemes, such as the AUSM-family and Roe's FDS [14], has been limited to low order interpolations. The two alternative Riemann solvers, Lax-Friedrichs and Roe's with an entropy fix, are also used in the following examples for a systematic comparison of stability, accuracy, and ultimately cost-effectiveness for very high order methods.

5 Boundary condition implementation

The implementation of boundary conditions could drastically alter overall accuracy in the final numerical solution. In this section, four implementations of reflective, slip wall boundary conditions are described and tested. The boundary conditions could be enforced at either cell nodes or cell edges. Here, we consider a grid with uniform spacing, in which the unknown variables V are given at cell centers. For our purposes, the physical domain boundary conditions are enforced at the cell edge locations. Therefore, all cell centers are interior to the domain and updated in the time advancement step, see Fig. 3.

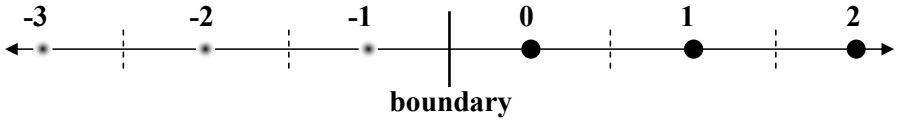

Figure 3: Schematic of cell-center nodes used in the solid-boundary condition: faded disk – Ghost node; solid disk – Cell node; dashed lines – Cell edges.

To preserve the interior update procedure near the boundaries, ghost nodes are used to pad the computational domain. These ghost nodes satisfy the particular type of boundary condition and update along with the interior nodes. Typical conditions are subsonic and supersonic inflow, outflow, and slip wall boundaries.

Ghost nodes across a reflective boundary have states symmetric to interior nodes normal to the boundary, with the exception of the normal component of velocity that is antisymmetric. Denoting $V=(\rho,\ u,\ v,\ p)^T$, we express the symmetry condition by

$$V_{-(j+1)}=V_j\ , \qquad \text{for } j=0,1,2.$$

On a vertical slip wall in the y-direction, the primitive and flux quantities must satisfy $V_w=[\rho_w,\ 0,v_w,p_w]^T$ and $F_w=[0,p_w,0,0]^T$ respectively, where the subscript "w" denotes the state at the wall. However, it is unclear how to set the other quantities $(\rho_w,\ v_w,\ p_w)$. This is the main reason the boundary implementation can lead to noticeably different results even though everything else remains the same. In what follows, we consider two approaches to ensure the satisfaction of V_w and F_w. Using the ghost node strategy and denoting the state on the exterior side of the wall by "L" and state on the interior side of the wall by "R", anti-symmetry is applied to the normal component velocity u, while other quantities follow the symmetry condition:

$$(\rho_L,\ u_L,\ v_L,\ p_L)=(\rho_R,\ -u_R,\ v_R,\ p_R), \tag{5.1}$$

or by hard enforcing $u_w=0$ at the boundary with $u_L=u_R=0$, i.e.,

$$(\rho_L,\ u_L=0,\ v_L,\ p_L)=(\rho_R,\ u_R=0,\ v_R,\ p_R). \tag{5.2}$$

The requirement that $u_w=0$ should be automatically enforced appropriately by the flux scheme. Then, $(\rho_w,0,v_w,\ p_w)$ can be obtained by solving the Riemann problem with either of the above pair of states.

Alternatively p_w could be solved directly, and the Riemann solver skipped, since it is all that is needed for a complete description of the flux F_w. The exact solution of the Riemann problem over the nonlinear field characteristic equation was used in [18].

$$\left(\frac{\partial u}{\partial t}\pm\frac{1}{\rho a}\frac{\partial p}{\partial t}\right)+(u\pm a)\left(\frac{\partial u}{\partial x}\pm\frac{1}{\rho a}\frac{\partial p}{\partial x}\right)=0. \tag{5.3}$$

Denoting i for the state on the interior side of the boundary, $i=L$ for upper boundary and $i=R$ for lower boundary, and associating them with + and – signs respectively, the exact solution of p_w is given below.

If $\pm u_i\leqslant 0$ (rarefaction wave):

$$p_w=p_i\left[1\pm\frac{(\gamma-1)u_i}{2a_i}\right]^{\frac{2\gamma}{\gamma-1}}. \tag{5.4}$$

If $\pm u_i>0$ (shock wave):

$$p_w=p_i+\frac{u_i}{2A_i}\left(u_i\pm\sqrt{{u_i}^2+4A_i(p_i+B_i)}\right), \tag{5.5}$$

where

$$A_i=\frac{2}{(\gamma+1)\rho_i},\qquad B_i=\frac{(\gamma-1)}{(\gamma+1)}p_i. \tag{5.6}$$

Liou [12] proposes an approximate solution to Eq. (5.3) by either

$$p_w^{n+1}=\frac{p_w^n+2\lambda p_i^{n+1}\left(\pm\gamma u_i^{n+1}+a_i^{n+1}\right)}{1+2\lambda a_i^{n+1}} \tag{5.7}$$

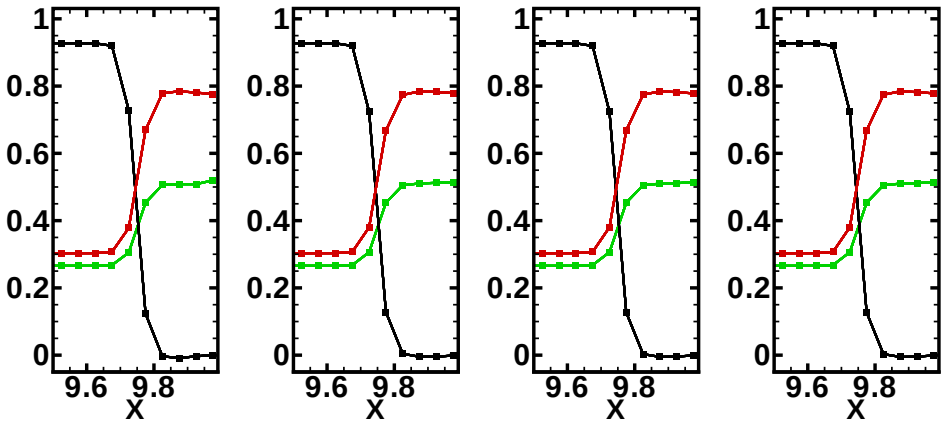

Figure 4: Effect of boundary implementation for 1D Sod problem after the right moving shock reflects off a slip wall using AUSM$^+$-UP. a) Eq. (5.2), b) Eq. (5.1), c) Eq. (5.8), d) Eqs. (5.4)-(5.5). Black: velocity; red: pressure; green: density.

or

$$p_w = p_i \pm u_i(\rho a)_i. \tag{5.8}$$

These are the low Mach number approximations of Eqs. (5.4) and (5.5), which is the case with a diminishing normal velocity near the wall.

Test cases in which shocks or other large gradients interact with the boundary prove to exhibit the largest discrepancy between implementations. Using ghost nodes, this situation is reminiscent of a collision between two shocks, and as seen in the 1D blast wave problem [12], could create inaccurate solutions. Fig. 4 is a section of the domain for the 1D Sod problem near a reflective upper boundary immediately after the right moving shock reflects off the slip wall.

6 Numerical tests and comparison

6.1 2D oblique shock reflection

The steady 2D oblique shock reflection problem has a known analytic steady state solution and is used to evaluate the issues discussed above: numerical flux, high order reconstruction, variables set, and boundary procedures. As shown in Fig. 5, all boundary treatments give similar well-behaved solutions, sharp and monotone representation of both shock waves, but MP gives a crisper resolution of shock wave than WENO5M. It is shown in Fig. 6 that explicitly setting the normal velocity component equal to zero at the reflective boundary raises the residual errors in both pressure and y-velocity compared to the other implementations; on the other hand, the convergence histories with both the exact and approximate characteristic boundary conditions are essentially identical. In

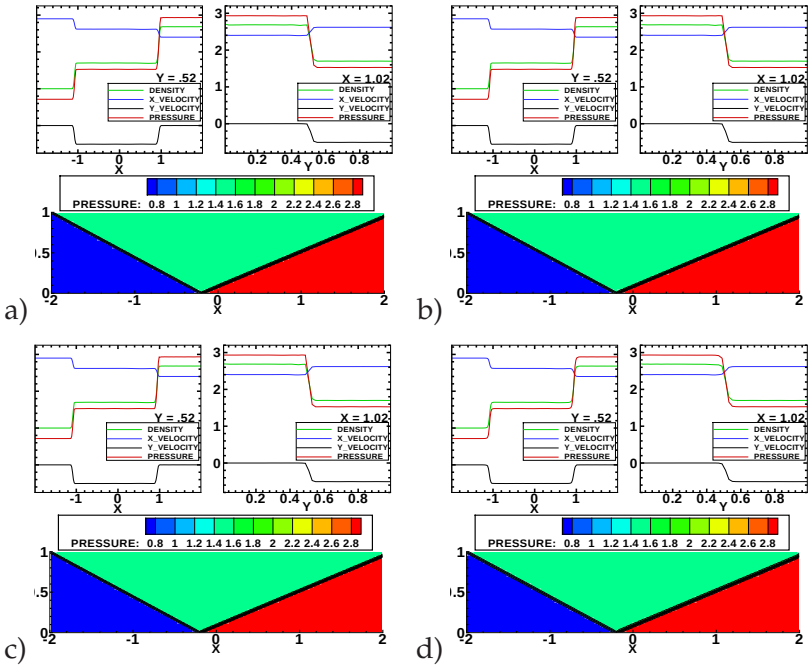

Figure 5: Effects of boundary implementation for 2D shock reflection using AUSM$^+$-UP, RK3, CFL$=0.4$, grid 200×50 and characteristic interpolation MP5 in a)-c). a) Eq. (5.2), b) Eq. (5.1), c) Eq. (5.8), d) using WENO5M [19] with Eq. (5.8).

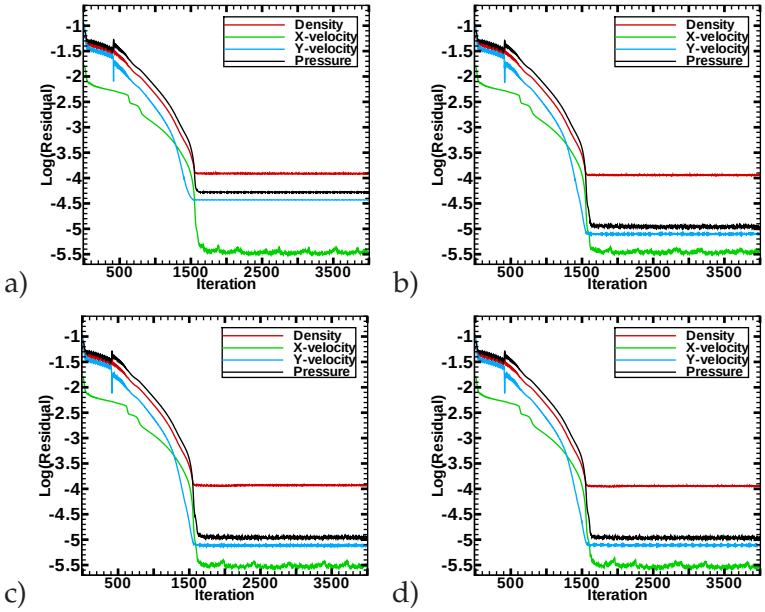

Figure 6: Effect of employing low Mach number scaling function f_a in Eq. (4.13) on the residual convergence for 2D shock reflection using characteristic interpolation MP5, AUSM$^+$-UP (steady), RK3, CFL$=0.4$. a) Eq. (5.2), b) Eq. (5.1), c) Eq. (5.8), d) Eqs. (5.4)-(5.5).

Fig. 7, the residual errors are shown for WENO5M and MP5 with and without consideration for steady shock convergence; we see the added benefit between using the steady form of AUSM$^+$-UP compared to the unsteady form. The solution using WENO5Z, not shown here, is indistinguishable from that of WENO5M. It is remarked that the AUSM$^+$-UP gives an improved solution over its predecessor, AUSM$^+$ (not shown), because it exhibits no oscillations in the transverse direction.

6.2 2D double mach reflection

The 2D double Mach reflection problem has been studied both computationally and theoretically [6]. It consists of a shock wave moving parallel to a flat surface and impinging onto an inclined ramp. For testing purposes, the domain geometry is modeled by rotating the frame so the ramp is horizontal and the incoming shock is oblique with the ramp angle, thus removing the need for an angled geometry. The flow is unsteady and develops a very distinct set of complex structures due to the three interacting incident, reflected, and Mach shocks. This is a test case where ROR or SEL corrections must be used for solutions with greater than 3^{rd} order accuracy when the AUSM$^+$-UP or Roe splitting with entropy fix are used. For these combinations, solvability issues arise at the location where the ramp meets the flat surface. In Fig. 8, this is toward the bottom left on the lower y-boundary where the reflected shock begins. When using the Lax-Friedrichs flux no solvability issues are experienced and therefore there is no need for invoking the corrections ROR or SEL.

For the double Mach reflection problem, AUSM$^+$-UP and Roe flux with entropy fix perform better with exact or approximate characteristic boundary conditions compared to those in Eqs. (5.1) and (5.2). For these latter boundary conditions, the schemes experience much more error earlier on and admit unsatisfactory solutions, especially on finer grids.

6.3 2D Rayleigh-Taylor problem

Next, we consider the Rayleigh-Taylor instability problem. While this is a classical problem and computed results have been reported extensively in the literature, there does not exist a known solution for the evolution of the flow. No quantitative validation is possible since the solution does not converge in the sense that more fine structures continually appear with finer grids. In Fig. 9, rows display differences between MP5 and WENO5M interpolations; columns display differences due to boundary condition implementation. Again, there is a clear difference in the predicted flow structures between these two interpolations. Fig. 10 shows richer details when the grid spacing is refined by three methods of AUSM$^+$-UP, Roe, and Lax-Friedrichs together with MP5 on three mesh sizes; there are recognizable differences in the results of finest grid. We also note that the numerical solution remains quite stable and regular, as manifested by its symmetry. In Fig. 11, we compare the AUSM$^+$-UP results between MP and WENO-M from 5^{th} to 13^{th} order of ac-

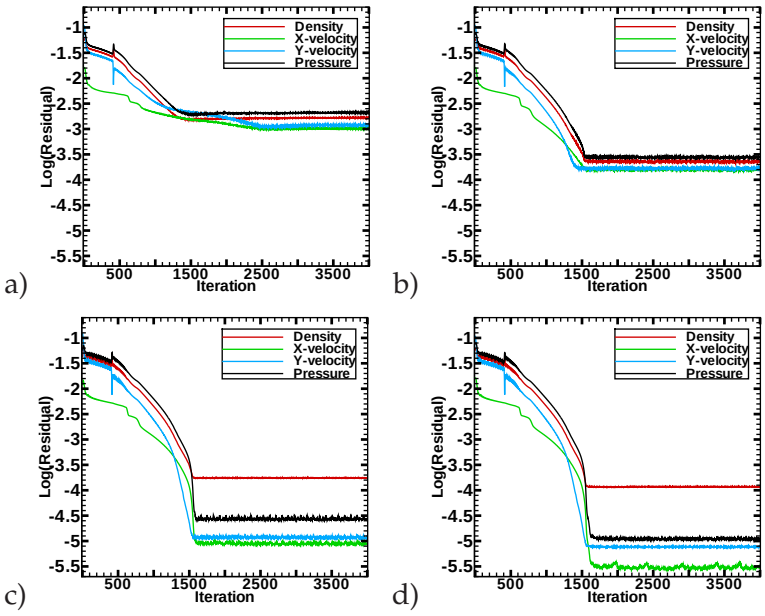

Figure 7: Effect of employing the low Mach number scaling factor for steady flow calculation of the 2D shock reflection problem. Top row: using WENO5M, a) unsteady, b) steady; Bottom row: using MP5, c) unsteady, d) steady. AUSM$^+$-UP, RK3, CFL=0.4, BC Eq. (5.8).

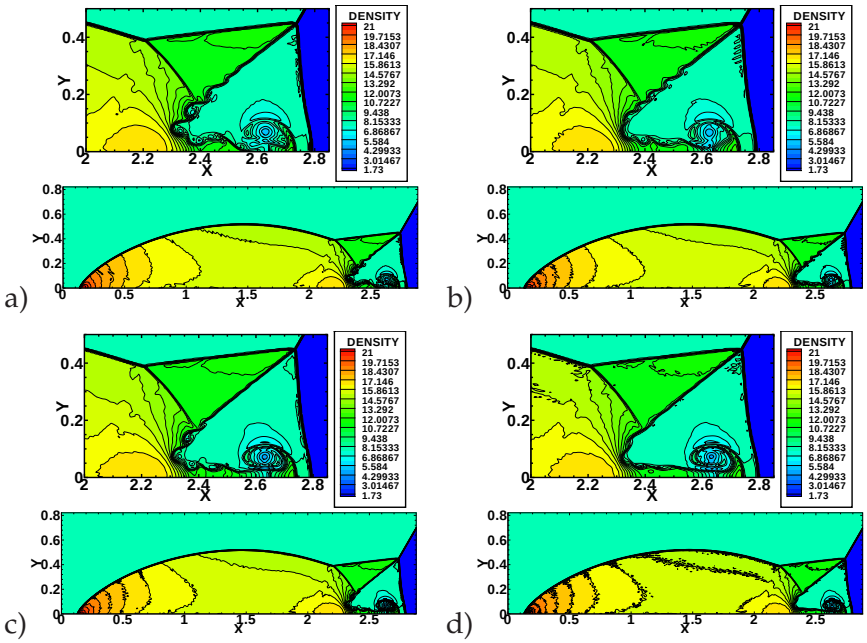

Figure 8: Effects of interpolation schemes and numerical fluxes for 2D Double Mach Reflection using characteristic variables, RK3, CFL=0.4, grid 960×240, and at t=0.2. a) MP7 and b) WENO7M both using BC Eq. (5.1), and Lax-Friedrichs flux, c) MP7 and d) WENO7M both using BC Eq. (5.8), and AUSM$^+$-UP (unsteady) with ROR.

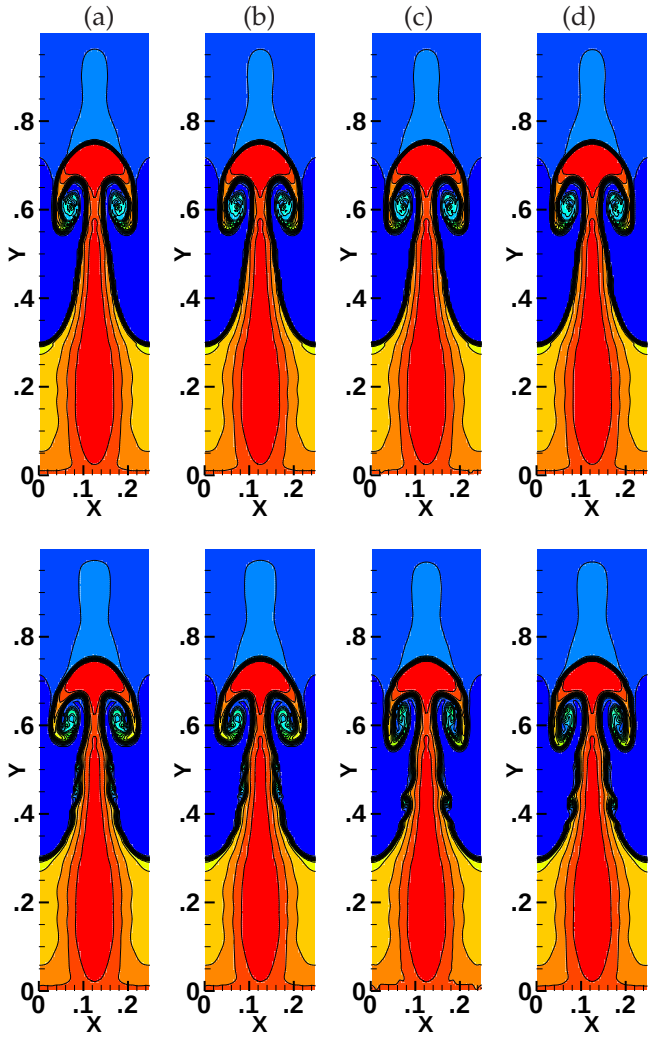

Figure 9: Effects of numerical boundary conditions for 2D Rayleigh-Taylor using two interpolation schemes, with AUSM$^+$-UP (unsteady), RK3, CFL$=0.4$, grid 60×240, and at $t=1.95$. Top: MP5; Bottom: WENO5M. a) Eqs. (5.4)-(5.5), b) (5.8), c) (5.2), and d) (5.1).

curacy. More complexities are observed by increasing accuracy, more so with MP than WENO-M.

6.4 2D 90-degree corner shock diffraction

The next test case is the calculation of a planar shock moving around a 90-degree corner, resulting in a sudden expansion of the flow near the foot of the shock along with additional flow features: a Mach-stem reflection at the backward-facing wall and a slip line emanating from the triple point, a complicated interior shock, and the leading shock be-

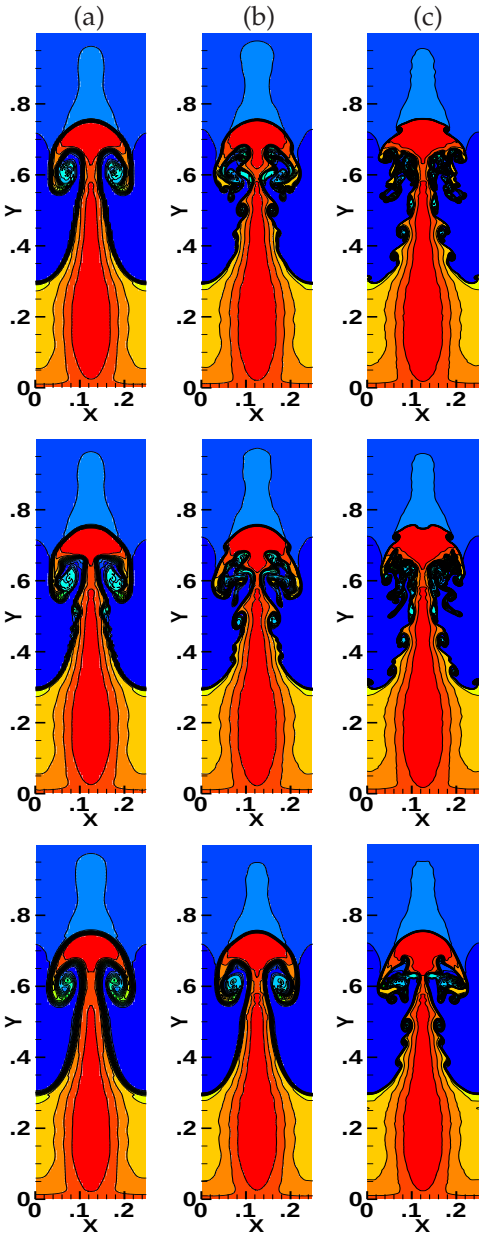

Figure 10: Effects of numerical fluxes and grid size for 2D Rayleigh-Taylor using MP5 characteristic variable interpolation, RK3, B.C. Eq. (5.8) CFL=0.4, t=1.95. Top: AUSM$^+$-UP (unsteady); Middle: Roe with Entropy Fix; Bottom: Lax-Friedrichs flux. a) grid 60×240, b) 120×480, c) 240×960.

ing morphed into a curved surface from the original planar one. This case is being used to test a numerical method's ability to handle a severe rarefaction and to resist forming so-called carbuncle phenomenon, which is a numerically induced shock instability. It is well

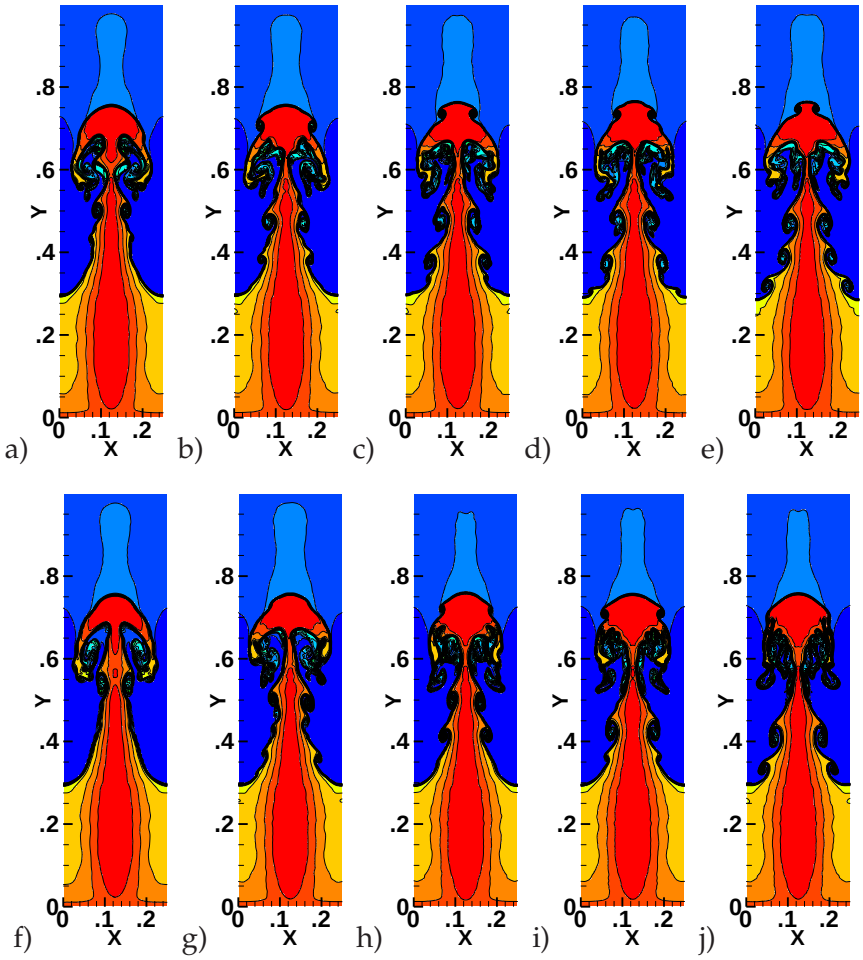

Figure 11: Effects of order of accuracy and interpolation schemes for 2D Rayleigh-Taylor using AUSM$^+$-UP (unsteady), characteristic variable interpolation, RK3, B.C. Eq. (5.8), CFL$=0.4$, grid 120×480, and at $t=1.95$: a) MP5, b) MP7, c) MP9, d) MP11, e) MP13; f) WENO5M, g) WENO7M, h) WENO9M, i) WENO11M, j) WENO13M.

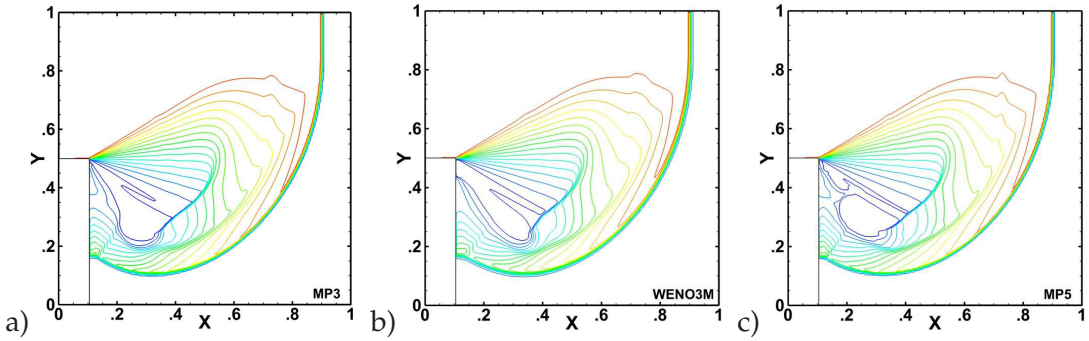

Figure 12: 90-Degree Corner Shock Diffraction using AUSM$^+$-UP (unsteady), characteristic variable interpolation, RK3, B.C. Eq. (5.8), CFL$=0.4$, grid 200×200, and at $t=0.1401$: a) MP3, b) WENO3M, c) MP5.

known that the Roe's splitting (even with an entropy fix) has produced such a problem. It is also equally known that the AUSM-family methods are free from this anomaly, as demonstrated in recent [11] and previous publications [9,10,12,13]. However, these tests were only done for first and second order accuracy with TVD limiters. Thus, it is of great interest to investigate whether the AUSM methods would be afflicted with the carbuncle difficulty when using high order interpolations. Fig. 12 gives the AUSM$^+$-UP solutions with MP3, WENO3-M and MP5; they all exhibit correct and clean solutions. MP3 gives features converging to MP5, while WENO3-M appears to lose sharpness of some interior features. It is noted that MP5 invokes a few isolated non-physical flux states as the shock first diffracts around the corner, hence necessitating the use of ROR or SEL.

6.5 1D shock-wave/entropy interaction

After seeing the benefits of using high order accurate interpolations, it is legitimate to consider two questions: (1) what is the ratio of overall cost to benefit for increasing order of accuracy, and (2) given a constant grid size, does there exist a limit on the added benefit by increasing order of accuracy? If such a limit exists, then how does it change when the grid size changes? For nonlinear problems, often containing discontinuities and varying length scales, it may not be adequate to resolve fine scales by simply increasing the order of accuracy; sufficiently fine grids must be made available to resolve smaller variations of interest. In this section, the added benefit due to increasing order of accuracy versus grid size is measured using the model problem of a 1D shock wave interacting with a train of entropy waves [17]. The solution involves both discontinuous and smooth but highly oscillatory profiles; see Fig. 13. The cost is defined as the total computation time to reach $t=4.0$ seconds. The L2 norm of density with respect to a highly refined solution (of 27,000 cells) is calculated over only the smooth but highly oscillatory portion, $1.0\leq x\leq 4.5$, so large errors at discontinuities are excluded.

Six grid sizes are used and the average number of cells per period of the highly oscillatory waves is summarized in Table 1. As an example with a grid size of 1,600 cells, there are approximately 11 cells per period, see Fig. 14. The results for the L2 norm, by AUSM$^+$-UP, with respect to the order of accuracy and grid size are plotted in Fig. 15;

Table 1: Number of cells per wave for various cell sizes.

Total cells	Average cells per period
500	4
1000	7
1600	11
3000	20
14,400	95
27,000	179

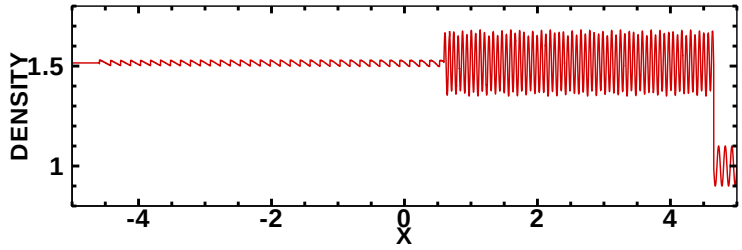

Figure 13: 1D Shock-Wave/Entropy Interaction of Titarev and Toro [17] at $t=4.0$. Grid-converged solution taken at 14,400 time steps for the 1,600-cell study and at 27,000 for the 3,000-cell study.

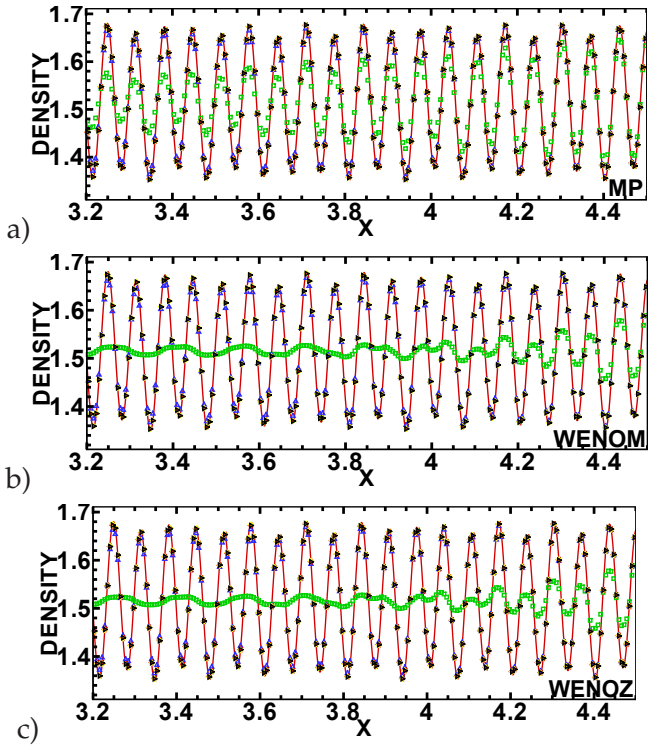

Figure 14: Comparison of solutions by three high order methods, a) MP, b) WENO-M, and c) WENO-Z, with different orders of accuracy on a grid of 1,600 nodes. Order: — converged, □ 3^{rd}, △ 5^{th}, ◁ 7^{th}, ◇ 9^{th}, ▷ 11^{th}.

three observations can be obtained. First, at 3^{rd} order, MP3 and the WENO3s[§] all perform the same on the coarsest grid, even though there are enough grid points to describe a wave. However, as grid is refined, MP3 performs increasingly better than the WENO3s. Second, at 5^{th} order and higher, MP and the WENOs are visually indistinguishable for all grid sizes. This suggests that the discrepancy due to grid size diminishes after a "sufficiently" high order of accuracy, and the improvement due to increasing order eventually

[§]By WENOs, we mean the two WENO variations WENO-M and WENO-Z cited in the references.

reaches a limit. This is evident in Fig. 15 for three grids, N=1,000, 1,600, and 3,000, in which each shows saturation in solution accuracy, with the limit near 7^{th} order on the finest grid and near 11^{th} order on the coarsest grid; this trend also makes sense, as a coarser grid requires a higher order interpolation to reach its asymptotic limit.

It is stressed that the grid size must be fine enough to resolve all the length scales in the flow structure. For further elucidation, we show in Fig. 16 the results on a grid of 500 cells, corresponding to approximately 4 cells per period, which can barely make out a wave. Clearly, both MP and WENO are not adequate to resolve the wave form despite using 13^{th} order of accuracy; the initial recognition of a wave form by the WENOs quickly smears out further downstream of the leading wave and MP is completely incapable of capturing the wave form. This suggests that the WENO interpolations are more dependent on order, while MP shows no improvement by increasing order if the problem is under-resolved.

To further quantify the merit of increasing order of accuracy, we suggest a cost-effective measure using the following function

$$\eta = \frac{1}{L2Norm \times Cost}. \tag{6.1}$$

Here the cost is the total computational time. This function increases, showing higher efficiency, when the cost and/or L2 norm decreases. Fig. 17 summarizes the efficiency of MP and the WENOs with accuracy from 3^{rd} to 11^{th} order on three grids. The MP scheme is clearly most efficient and the WENO-Z has a slight advantage over the WENO-M. Interestingly, all three schemes have a similar trend on each grid size (solid lines vs. dotted lines). Each has reached a maximum efficiency (e.g., 5^{th} order for WENO and 7^{th} order for MP on the grid of 3,000 cells), a limit of no return, after which the efficiency decreases again because the higher order procedures cost more to compute with no added accuracy. In addition, the maxima are delayed to higher order when a coarser grid is used, as expected.

7 Conclusion

In conclusion, we have investigated the use of AUSM$^+$-UP with two approaches of arriving at high order accuracy, weighted essentially nonoscillatory (WENO) and monotonicity preserving (MP) schemes; for the former we use two recent variants, WENO-M and WENO-Z, in the present study. It is found that using local characteristic variables of Euler equations is preferred for interpolation because it removes over/under shoots and oscillations at locations with discontinuities, and reflecting boundaries. Also, the wall pressure given by following approximate characteristics, Eq. (5.8), promotes better residual convergence for steady state solutions and is just as effective as the exact characteristic extrapolation, Eqs. (5.4)-(5.5). The AUSM-based high order scheme is found to behave robustly and accurately, at least as well as the Lax-Friedrichs and Roe schemes,

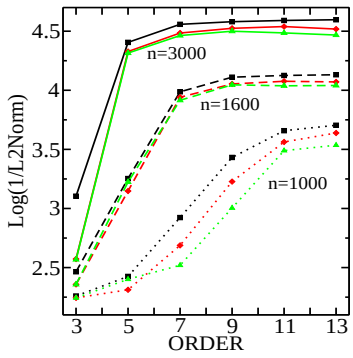

Figure 15: L2-Norm of density errors relative to the highly resolved solution, with respect to order of accuracy on three grids. ■ MP, ♦ WENO-M, ▲ WENO-Z.

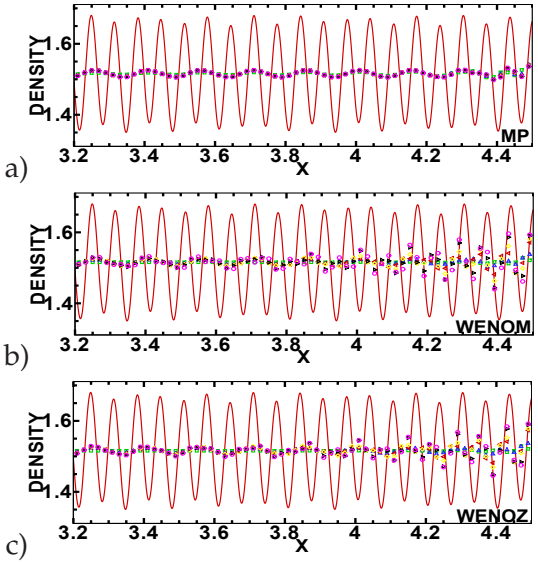

Figure 16: Comparison of solutions by three high order methods, a) MP, b) WENO-M, and c) WENO-Z, with different orders of accuracy on a grid of 500 nodes. Order: — converged, □ 3^{rd}, △ 5^{th}, ◁ 7^{th}, ◇ 9^{th}, ▷ 11^{th}, ○ 13^{th}.

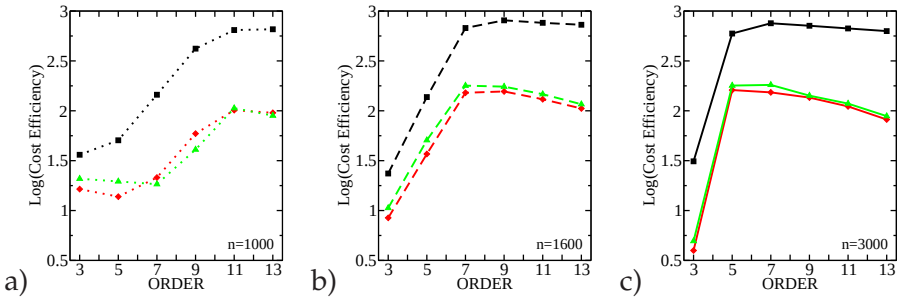

Figure 17: Comparison of efficiencies, Eq. (6.1), by ■ MP, ♦ WENO-M, ▲ WENO-Z, with respect to order of accuracy on three grids $n=1{,}000$, $1{,}600$, and $3{,}000$ respectively.

for several complex flow problems. AUSM$^+$-UP is also found to be free of shock instability (a.k.a. carbuncle phenomenon). Even though as high as 13^{th} order has been employed, we conclude that pushing ever-higher order is not beneficial, as a limit of no further improvement in accuracy or efficiency will be reached for a given grid resolution. In other words, to aspire for higher and higher accuracy, for better convergence of a discrete solution to that of the differential equations, the grid must be continuously refined together with employing higher order interpolations.

Acknowledgments

This work has been supported by the Subsonic Fixed Wing and Supersonics Projects under the NASA's Fundamental Aeronautics Program, Aeronautics Mission Directorate. We also thank H.T. Huynh of NASA Glenn Research Center for his help with the MP method.

References

[1] D.S. Balsara and C.-W. Shu, Monotonicity preserving weighted essentially non-oscillatory schemes with increasingly high order of accuracy. J. Comput. Phys., 160 (2000), 405-452.
[2] R. Borges, M. Carmona, B. Costa, and W.S. Don, An improved weighted essentially non-oscillatory scheme for hyperbolic conservation laws. J. Comput. Phys., 227 (2008), 3191-3211.
[3] G.A. Gerolymos, D. Senechal, and I. Vallet, Very-high-order WENO schemes. AIAA Aerospace Science Meeting, 47 (2009).
[4] S.K. Godunov, A finite difference method for the numerical computation of discontinuous solutions of the equations of fluid dynamics. Mat. Sb., 47 (1959), 357-393.
[5] A. Harten, High resolution schemes for hyperbolic conservation laws. J. Comput. Phys., 49 (1983), 357-393.
[6] L.F. Henderson, E.I. Vasilev, G. Ben-Dor, and T. Elperin, The wall-jetting effect in mach reflection: Theoretical consideration and numerical investigation. J. Fluid Mech., 479 (2003), 259-286.
[7] A.K. Henrick, T.D. Aslam, and J.M. Powers, Mapped weighted essentially non-oscillatory schemes: Achieving optimal order near critical points. J. Comput. Phys., 207 (2005), 542-567.
[8] G.-S. Jiang and C.-W Shu, Efficient implementation of weighted ENO schemes. J. Comput. Phys., 126 (1996), 202-228.
[9] M.-S. Liou, A sequel to AUSM, part II: AUSM+-up for all speeds. J. Comput. Phys., 214 (2006), 137-170.
[10] M.-S. Liou, A sequel to AUSM: AUSM+. J. Comput. Phys., 129 (1996), 364-382.
[11] M.-S. Liou, Open problems in numerical fluxes: Proposed resolutions. In 20th AIAA Computational Fluid Dynamics Conference (2011).
[12] M.-S. Liou, Progress towards an improved CFD method: AUSM+. AIAA paper 1995-1701-CP, in 12th AIAA Computational Fluid Dynamics Conference (1995).
[13] M.-S. Liou and C.J. Steffen Jr., A new flux splitting scheme. J. Comput. Phys., 107 (1993), 23-39.
[14] P.L. Roe, Approximate Riemann solvers, parameter vectors, and difference schemes. J. Comput. Phys., 43 (1981), 357-372.

[15] C.-W. Shu and S. Osher, Efficient implementation of essentially non-oscillatory shock capturing schemes. J. Comput. Phys., 77 (1988), 439-471.
[16] A. Suresh and H.T. Huynh, Accurate monotonicity-preserving schemes with Runge-Kutta time stepping. J. Comput. Phys., 136 (1997), 83-99.
[17] V.A. Titarev and E.F. Toro, Finite-volume WENO schemes for 3-D conservation laws. J. Comput. Phys., 201 (2004), 238-260.
[18] J.J.W.van der Vegt and H.van der Ven, Slip flow boundary conditions in discontinuous Galerkin discretizations of the Euler equations of gas dynamics. World Congress on Comput. Mech., 5 (July 7-12 2002).
[19] S. Zhang and C.-W. Shu, A new smoothness indicator for the WENO schemes and its effect on the convergence to steady state solutions. J. Sci. Comput., 31 (2007), 273-305.